JGR Planets

RESEARCH ARTICLE
10.1029/2019JE006191

Key Points:
- The perceived thicknesses of aeolian cross sets are increased (and their distributions altered) due to remote sensing resolution limits
- Image resolution limits can severely alter interpretations of aeolian sandstones, even at HiRISE resolution (best available at 25 cm/pixel)
- Accurate measurements from HiRISE images require outcrop slopes less than 13°, such that thin sets are exposed over detectable distances

Correspondence to:
B. T. Cardenas,
bencard@caltech.edu

Citation:
Cardenas, B. T., Swanson, T., Goudge, T. A., Wagner, R. W., & Mohrig, D. (2019). The effect of remote sensing resolution limits on aeolian sandstone measurements and the reconstruction of ancient dune fields on Mars: Numerical experiment using the Page Sandstone, Earth. *Journal of Geophysical Research: Planets*, *124* 3244–3256. https://doi.org/10.1029/2019JE006191

Received 10 SEP 2019
Accepted 14 NOV 2019
Accepted article online 22 NOV 2019
Published online 3 DEC 2019

The Effect of Remote Sensing Resolution Limits on Aeolian Sandstone Measurements and the Reconstruction of Ancient Dune Fields on Mars: Numerical Experiment Using the Page Sandstone, Earth

Benjamin T. Cardenas[1,2], Travis Swanson[3], Timothy A. Goudge[1], R. Wayne Wagner[4], and David Mohrig[1]

[1]Jackson School of Geosciences, University of Texas at Austin, Austin, TX, USA, [2]Now at Division of Geological and Planetary Sciences, California Institute of Technology, Pasadena, CA, USA, [3]Department of Geology and Geography, Georgia Southern University, Statesboro, GA, USA, [4]Department of Civil and Environmental Engineering, University of New Orleans, New Orleans, LA, USA

Abstract The distribution of cross-set thicknesses is important data for reconstructing ancient aeolian dune fields from the strata they accumulated, but most aeolian strata on Mars must be observed from satellite. We hypothesize that remote sensing resolution limits will affect cross-set thickness measurements and the dune-field reconstructions that follow. Here we test this hypothesis using a numerical experiment mimicking the effects of satellite image resolution limits performed on a distribution of aeolian cross-set thicknesses measured in the field from the Jurassic Page Sandstone, Arizona, USA. Page set thicknesses are exponentially distributed, representing the accumulations of dry dune fields (no water table interactions with the dunes) in a state of net-sediment bypass. When observed from satellite, set-thickness measurements increase as adjacent sets become indistinguishable, based on the map-view distance between their upper and lower bounding surfaces. This is termed the *exposure distance* of a cross set and is a function of (1) the set thickness, (2) the dip of the outcrop surface, and (3) the number of satellite image pixels required to detect a set (detection limit). By running experiments using outcrop dips from 1° to 60° and detection limits from 0.75 to 2.50 m (3 to 10 High-Resolution Imaging Science Experiment pixels), we find that gently sloping surfaces (< 13°) at all detection limits are associated with the least blending of adjacent sets, conserving the net-bypass interpretation made from the true set thicknesses. Although these results are specific to the Page, they can be used as a guide for future Mars work.

Plain Language Summary Cross sets are sedimentary deposits left by wind-blown sand dunes. Cross sets can be preserved for long amounts of time as sedimentary rocks, where variability in their thickness can be analyzed to understand the motion of ancient dunes and the processes that helped the dunes move, including ancient winds, the presence or lack of near-surface groundwater, ancient topography, and tectonics. On Earth, we can accurately measure cross-set thicknesses in the field, but for Mars we are mostly limited to satellite images. Here we mimic the uncertainties present in a satellite image of Mars by altering field-measured thicknesses from Earth. We perform this numerical experiment on field-measured cross-set thicknesses from the Page Sandstone, Arizona. The altered thicknesses are checked for how they might affect our understanding of the ancient Page dune fields. Based on these experiments, satellite images offer a risk of misinterpretation, but good measurements can be made at High Resolution Imaging Science Experiment image resolution if the slope of the rock outcrop is shallow, 13° from horizontal or less. At these shallow slopes, the thinnest cross sets are exposed over long distances, making them detectable from orbit. Though these results are specific to the Page, they can help guide future Mars work.

1. Introduction

The thickness distributions of aeolian cross sets are among the easiest stratigraphic data to collect, and the shape of the distribution, as well as its statistical moments, records the aggradation, migration, and the size of dunes in a field (Bridge, 1997; Bridge & Best, 1997; Cardenas et al., 2019; Jerolmack & Mohrig, 2005; Paola & Borgman, 1991; Rubin & Hunter, 1983; Swanson et al., 2019). Wind is the dominant driver of sediment

transport on modern Mars (Ewing et al., 2010; Fenton & Hayward, 2010; Silvestro et al., 2011; Silvestro et al., 2013; Chojnacki et al., 2015; Day & Kocurek, 2016; Lapotre et al., 2016; Cornwall et al., 2018 and Cornwall et al., 2018; Chojnacki et al., 2019) and has likely been significant throughout the planet's history (e.g., Anderson et al., 2018; Banham et al., 2018; Day & Catling, 2018; Day & Catling, 2019; Grotzinger et al., 2005; Kite et al., 2013; Lewis et al., 2008; Lewis et al., 2008; Milliken et al., 2014). On Earth, the aeolian rock record dates back at least as far as the Archean (3.2 Ga, Rodríguez-López et al., 2014) and often records complex interactions of dunes with changing winds, topography, groundwater, tectonics, other dunes, and even life (e.g., Blakey et al., 1996; Brothers et al., 2016; Cardenas et al., 2019; Day & Kocurek, 2017; Havholm et al., 1993; Kocurek & Day, 2018; Loope, 2006). Therefore, aeolian strata are likely to provide a rich source of information about conditions at the ancient surface of Mars. This information is encoded particularly well into cross-set thicknesses (Cardenas et al., 2019; Jerolmack & Mohrig, 2005; Paola & Borgman, 1991; Swanson et al., 2019). Aeolian cross sets are observable on Mars from remote sensing images and digital elevation models (DEMs; e.g., Milliken et al., 2014; Anderson et al., 2018; Day & Catling, 2019), but we hypothesize that resolution limits could lead to remotely measured thickness distributions that are not representative of the true distribution. If so, this may lead to misinterpretations of the stratigraphy and the ancient Martian surface environment. The best currently available remote sensing images and stereo-derived DEMs of Mars come from the High Resolution Imaging Science Experiment (HiRISE) camera and have a spatial resolution of 0.25 (images) and 1 m/pixel with ~0.2-m vertical precision (DEMs) (Kirk et al., 2008; McEwen et al., 2007). However, this is still coarse relative to field observations, and these limits may have an effect on measurements of set thicknesses and the dune field reconstructions based on them.

Here we perform a numerical experiment using a field-acquired distribution of aeolian cross-set thicknesses from the Jurassic middle Page Sandstone, Arizona, USA (Cardenas et al., 2019) to determine how changes in satellite resolution affect the interpretation of the dune field. The detectability of a set is based on its thickness, outcrop dip, the size of a remote sensing image pixel, and the number of pixels needed to identify a unique set of cross strata. In this experiment, the observed population of cross-set thicknesses is modified as the dip of the outcrop surface and the number of pixels required to distinguish a set increase, and thinner sets go undetected and are visually blended into thicker, detected sets. The distributions of cross-set thicknesses are characterized using statistical moments (mean, standard deviation, and products thereof), distribution shapes, and the number of detected sets. The ancient environment and dune-field dynamics recorded by the Page Sandstone are well characterized (Cardenas et al., 2019; Swanson et al., 2019), and we compare these *true* characterizations to reinterpretations based on the experimental, resolution-limited distributions. To judge the significance of these altered interpretations, we compare the experimental results to data from the Jurassic Entrada Sandstone, which represents an opposite end-member wet dune-field accumulation to the dry Page dune fields. The goal of this contribution is to enable quantitative measurements of aeolian strata on Mars that take appropriate caution during interpretation and to provide guidance on minimizing this potential source of error.

1.1. Reconstruction of Dune-Field Kinematics From Cross-Set-Thickness Distributions

In aeolian dune fields, the controls on dune cross-set accumulation represent a mix of naturally occurring processes inherent to aeolian sedimentary systems (autogenic processes) and external, environmental forcings. Autogenic processes include dune interactions (Day & Kocurek, 2017, 2018; Ewing & Kocurek, 2010a, 2010b) and natural variation in dune scour depths (Bridge & Best, 1997; Cardenas et al., 2019; Jerolmack & Mohrig, 2005; Paola & Borgman, 1991; Swanson et al., 2019). Environmental forcings or boundary conditions include wind regime, atmospheric conditions, sediment availability and source geometry, basin geometry, the proximity of the water table to the surface, and antecedent topography (Kocurek et al., 2010; Cardenas et al., 2019; Chojnacki et al., 2019; Ewing et al., 2015; Swanson et al., 2019).

Net-bypass dune fields are able to accumulate and preserve cross sets via the filling of their own variably deep dune trough scours that form as the dunes migrate, without the need for net-bed aggradation (Paola & Borgman, 1991). These cross sets are laterally discontinuous, as they primarily represent the fill of the deepest local scours. This favors the preservation of thin, heavily scoured sets and thick, scour-filling sets. As such, the variability in set thickness is greater than the variability in dune scour depths. In contrast, laterally continuous, climbing cross sets record steady bed aggradation and will not favor the preservation of cross sets filling the deepest scours strongly, meaning a greater percentage of dunes have preserved cross sets

(Allen, 1973; Bridge & Best, 1997; Jerolmack & Mohrig, 2005; Leclair et al., 1997; Rubin & Hunter, 1982; Swanson et al., 2019). As a result, the variability in cross-set thickness is closer to the variability in dune scour depths.

To better understand the relative contributions of scour depth and bed aggradation, and therefore the forcings upon the dune field, the distribution of cross-set thicknesses can be analyzed quantitatively (Bridge & Best, 1997; Cardenas et al., 2019; Jerolmack & Mohrig, 2005; Leclair et al., 1997; Swanson et al., 2019). Dune heights are commonly gamma distributed, independent of setting—for example, fluvial, Paola and Borgman (1991); natural and experimental fluvial, van der Mark et al. (2008); experimental fluvial, Ganti et al. (2013); and aeolian, Swanson et al. (2016). With gamma distributed dune heights, a dune field undergoing net bypass will have a set thickness coefficient of variation of cross-set thicknesses, c_v, of 0.88 ($\pm$ 0.03) (Bridge, 1997; Jerolmack & Mohrig, 2005; Paola & Borgman, 1991), where

$$C_v = S_\sigma / S_m \tag{1}$$

and s_m and s_σ are the mean and standard deviation of set thicknesses. The value of c_v for a given dune field is controlled by the ratio of dune migration rate to bed aggradation rate (Bridge & Best, 1997; Cardenas et al., 2019; Jerolmack & Mohrig, 2005; Leclair et al., 1997; Paola & Borgman, 1991). The distribution of set thicknesses resulting from such a net-bypass dune field will be exponentially distributed (Cardenas et al., 2019; Jerolmack & Mohrig, 2005; Paola & Borgman, 1991; Swanson et al., 2019). With a higher aggradation rate relative to the dune migration rate, the set thickness c_v will decrease until it reaches the coefficient of variation of the original bedform heights (Jerolmack & Mohrig, 2005) in the range of 0.29–0.60 (White Sands Dune Field = 0.29, Swanson et al., 2016; Algodones Dunes = 0.45, Cardenas et al., 2019; and fluvial dunes = 0.60, Jerolmack & Mohrig, 2005). As the c_v decreases, the best fit distribution of set thicknesses will also change to a gamma distribution (Figure 1a). As the rate of bed aggradation approaches the rate of dune migration, this curve will also better represent the formative bedform heights (Jerolmack & Mohrig, 2005).

1.2. The Page and Entrada Sandstones, Earth

We use the Page and Entrada Sandstones, described below, as end-member aeolian dune-field strata, representing dry, net bypass (no water table; Page) and wet aggradation (water table; Entrada). The Jurassic middle Page Sandstone (hereafter, middle Page) is the record of at least six stacked aeolian dune fields, each in a state of near bypass (i.e., low sediment-accumulation rates/low aggradation) during which there was not a near-surface water table. Each net-bypass accumulation is separated from the others by formation-scale erosional surfaces (Blakey et al., 1996; Cardenas et al., 2019; Havholm et al., 1993; Havholm & Kocurek, 1994). Episodic highstands in dune field water table, driven by highstands in the adjacent Carmel Sea, helped preserve these net-bypass accumulations over long enough periods of time to subside the strata deeply enough to promote burial instead of reworking during the following episode of aeolian sedimentation following the next fall in Carmel Sea level (Blakey et al., 1996; Cardenas et al., 2019; Havholm et al., 1993). The net-bypass state of the middle Page is recorded by the set thickness c_v of 0.90 and the exponential distribution of set thicknesses (Cardenas et al., 2019). Additionally, the distribution of dune heights has been reconstructed for the middle Page and can be reconstructed from any set of net-bypass strata with reasonable assumptions about the standard deviation of the dune heights (Cardenas et al., 2019). In contrast with the Page, in the Jurassic Entrada dune fields, a rising near-surface water table drove significant dune field aggradation even after antecedent topography was filled (Crabaugh & Kocurek, 1993; Kocurek & Day, 2018). This is represented by a dominance of climbing and downlapping architectures and interdune sabkha deposits throughout (Crabaugh & Kocurek, 1993; Kocurek & Day, 2018). Most significantly for this study, the state of net aggradation is also recorded by the set thickness gamma-shaped distribution and c_v of 0.46, both of which sit in contrast to the middle Page (in the study area of Kocurek & Day, 2018; Cardenas et al., 2019).

2. Methods

We began with a population of field-acquired set thicknesses from the middle Page Sandstone (set thickness $n = 402$; data from Cardenas et al., 2019). The c_v of middle Page sets is 0.90 (equation 1; $s_m = 2.44$ m, $s_\sigma = 2.20$ m, minimum and maximum thicknesses of 0.16 and 15.75 m). The distribution was not rejected as exponential or gamma by two-sample Kolmogorov-Smirnov tests comparing the distribution to randomly generated

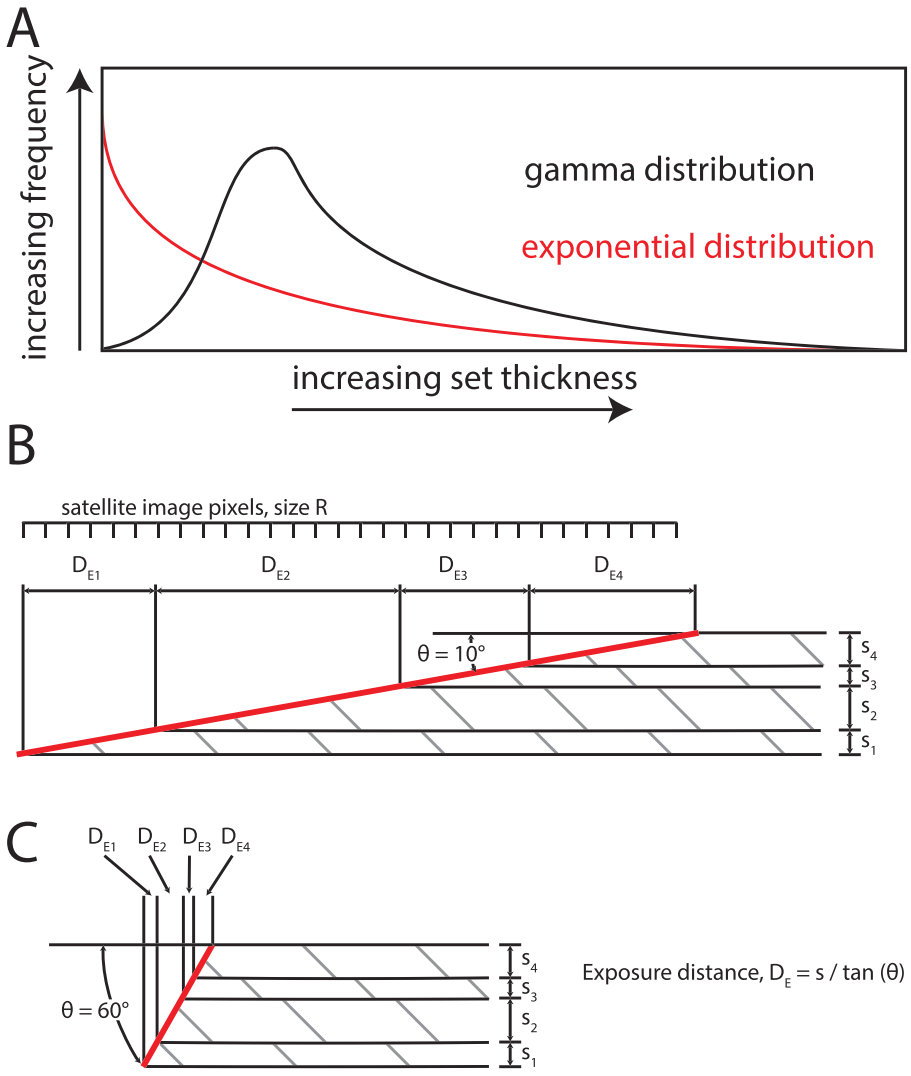

Figure 1. (a) Probability density function curves of exponential and gamma set-thickness distributions. Set thicknesses from net-bypass dune fields are exponentially distributed (Paola & Borgman, 1991) and become increasingly gamma distributed with increasing aggradation rates (Jerolmack & Mohrig, 2005). (b) Experiment schematic showing why exposure distance, D_E, is a function of outcrop dip (red surface, $\theta = 10°$) and cross-set thickness, s. Satellite resolution, R, is shown in relation to D_E. (c) An increased outcrop dip ($\theta = 60°$) results in decreased D_E for the same s values as Figure 1a. The formula to calculate D_E is shown, assuming horizontal strata.

distributions of size $n = 100$. Both the c_v and the exponential distribution are diagnostic of the net-bypass dynamics of the ancient Page dune fields. We tracked any changes in c_v and distribution shape as we modified the collection of set thicknesses to represent limitations imposed on the measurements as if they were collected using remote sensing data.

The population of Page set thicknesses was modified by removing measurements below detectable thresholds in remote sensing images and adding their thickness into adjacent sets. To perform this *blending* process, a value was calculated for each set called exposure distance, D_E, such that

$$D_E = s/\tan(\theta) \tag{2}$$

This represents the projection of the vertical set thickness into a surface of dip θ in degrees from horizontal. For a given set thickness s, D_E increases toward the total width of the set as the outcrop dip θ decreases. That is, a set of s thickness is exposed across a longer horizontal distance D_E where the dip of the outcrop is

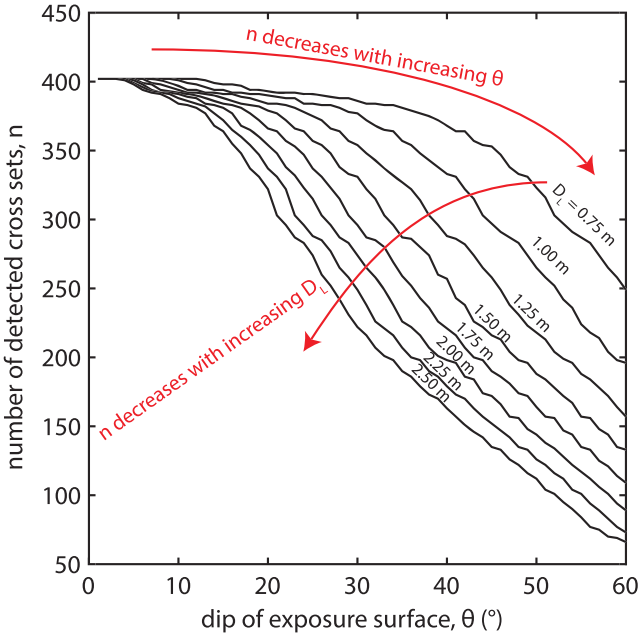

Figure 2. The effect of blending sets (Figure 1) on the number of detected sets (n), as a function of the dip of the exposure surface (θ) and the detection limit (D_L). The number of detected sets (n), and thus the degree of change from the original data set, is largely controlled by θ, which also amplifies the effect of D_L at high θ. Wiggles in the lines are due to the threshold nature of the resolution-based set-thickness blending.

shallower (Figures 1b and 1c). Importantly, as defined in Figure 1 and used in equation 2, s is the apparent set thickness. In the experiments presented here, we assumed all individual cross sets were consistently thick at the location of a single vertical section and horizontal so the apparent and true thicknesses were equal no matter the value of θ or the orientation of the exposure surface versus the paleo-transport direction of the cross set. This necessary simplifying assumption is partly appropriate for the cross sets of the Page Sandstone, as the formative dunes did not consistently climb (Cardenas et al., 2019). However, Page cross sets are not consistently thick between sections, and so are not necessarily consistently thick at one location with a changing θ.

If the strata are inclined at an angle Φ below the horizontal, equation 2 must be modified to use a true thickness that is different from the apparent thickness:

$$D_E = s_{\mathrm{TRUE}} \sin(\theta)/\tan(\theta) \cos(90–\Phi–\theta) \tag{2a}$$

With sufficient exposure, Φ can be measured using a DEM (e.g., Goudge et al., 2017; Hughes et al., 2019; Kite et al., 2016), in addition to the readily measured surface slope, θ. Equation 2 was run with a range from 1° to 60° at 1° intervals. Then, we defined a detection limit, D_L, such that

$$D_L = xR \tag{3}$$

where R is the size of an image pixel (set here as the minimum size of a HiRISE pixel, 0.25 m) and x is an assumed number of pixels required to identify a unique set. We set x to a range from 3 to 10 pixels at 1 pixel intervals, leading to D_L values ranging from 0.75 to 2.50 m at 0.25 m intervals. The length of three pixels is a typical rule of thumb for image detection limits and was a reasonable lower bound to begin exploration of results. With eight detection limits and 60 dips, 480 unique experiments were run. Although the range of surface dips was high, aeolian cross sets and their set-bounding surfaces are potentially identifiable across this entire range. For example, planform bounding surfaces are identified on Earth in Brothers et al. (2016), their Figure 4; near-planform sets on Mars are identified in Anderson et al. (2018), their Figures 3c and 3d; steeper exposures on Mars are identified by Milliken et al. (2014), their Figures 1c and 1d. Finally, although stereo-pair DEM resolution tends to be 4 times coarser than visible images, this experiment assumed subpixel interpolations of elevation are not the limiting factor in the collection of set-thickness measurements, and so was not considered.

Forty-five vertical sections containing a total of 402 set-thickness measurements through the middle Page Sandstone from Cardenas et al. (2019) were utilized in this experiment. For each section, the sets were tested for detection in order. For any given set, if $D_E \geq D_L$, that set was not modified. If $D_E < D_L$, then the set's thickness was added to adjacent sets depending upon its position, a process we define as blending, and then removed. If the first set was not detected, its thickness was added to the second. If the final set was not detected, its thickness was added to the previous set. If the set was between other sets, half of its thickness was added to the two adjacent sets. If the set was the only set in the section, it was labeled an automatic detection. One change was allowed to each section before another detection test was performed, until all sets passed the detection test. This process is analogous to the loss of subresolution data, as set thicknesses are blended together while overall section thickness is conserved.

3. Results

Of the 480 unique experiments, 430 (90%) produced data sets that, as hypothesized, were altered from the original as a result of our experimentally produced remote sensing resolution limitations. As outcrop dip (θ) increases, D_E for all sets decreases, dropping many sets below D_L. This leads to a decrease in the total number of detected sets, n, from the original 402 (Figure 2). Because the thickness of each of the 45

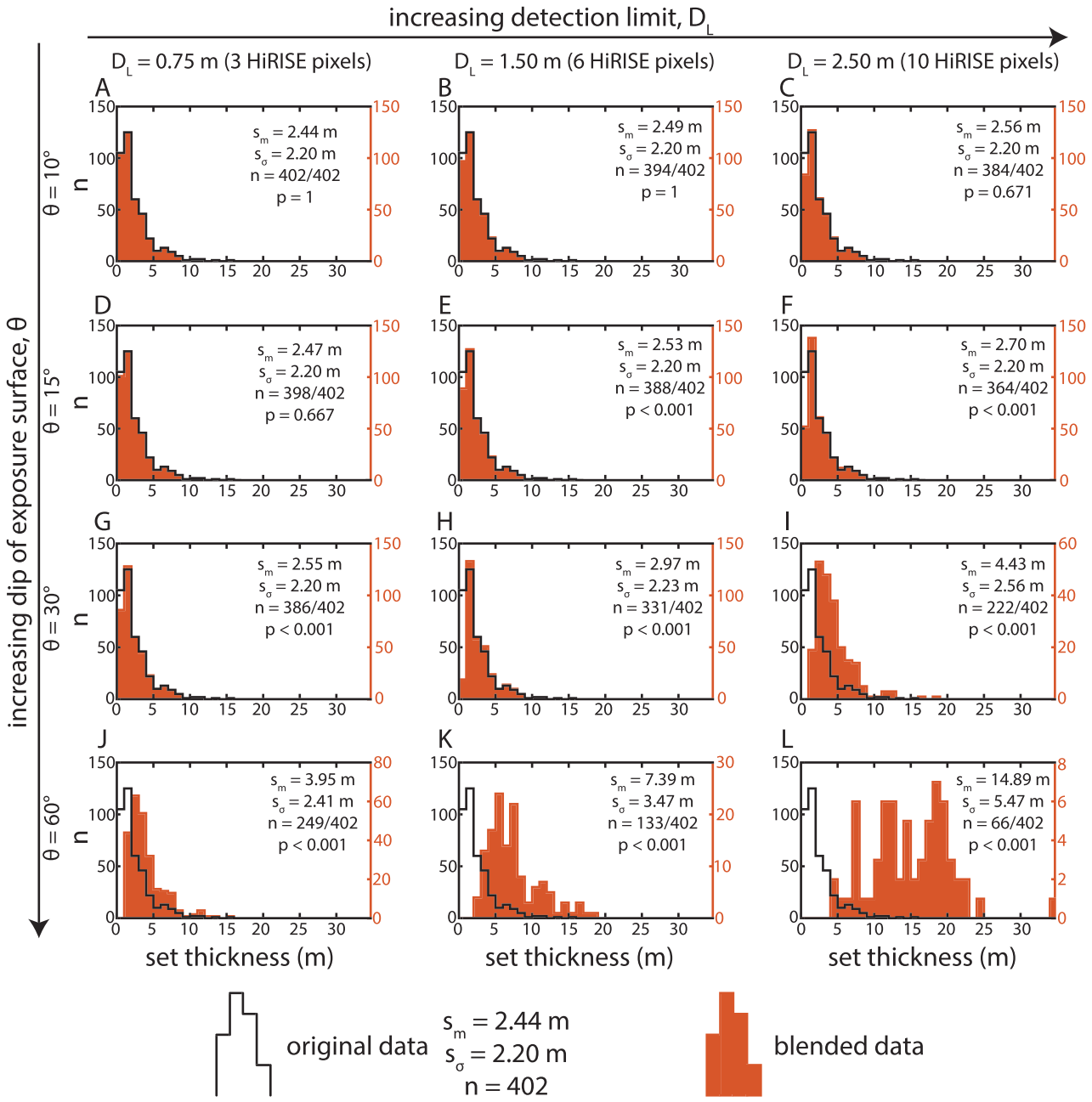

Figure 3. (a–l) Histograms comparing the original distribution of Page set thicknesses (black line) to 12 blended distributions (red filled). All histograms have two *y* axes showing *n* for the original data (left) and blended data (right), and 1-m bins. The blending of thin sets into adjacent sets is performed as a function of outcrop dip and assumed detection limits (Figure 1). Each panel shows the blended data's mean, standard deviation, *n*, and *p* value in comparison to the original data set, calculated using a two-sample Kolmogorov-Smirnov test. Columns represent experimental results at detection limits (D_L) = 0.75, 1.50, and 2.50 m (3, 6, and 10 HiRISE pixels). Rows represents results at exposure dips (θ) of 10°, 15°, 30°, and 60°. In general, increases in D_L and θ create blended data sets of decreasing similarity to the original, both in terms of shape, statistical moments, and number of measurements.

vertical sections is preserved, a decrease in *n* is concurrent with an observed thickening of some sets and an increase in the mean of observed set thickness. In the D_L = 0.75 m (three HiRISE pixels) scenario, the first decrease in *n* is at θ = 13°, and *n* drops as low as 249 (62% of original measurements) at 60° (Figure 2). The loss of the first set occurs at only θ = 4° in the D_L = 2.50 m (10 HiRISE pixels) scenario, and *n* is reduced to only 66 sets (16% of original measurements) in the θ = 60° experiment. The decrease in *n* preferentially drives an underrepresentation of the thinner side of the distributions, represented by the shrinking of

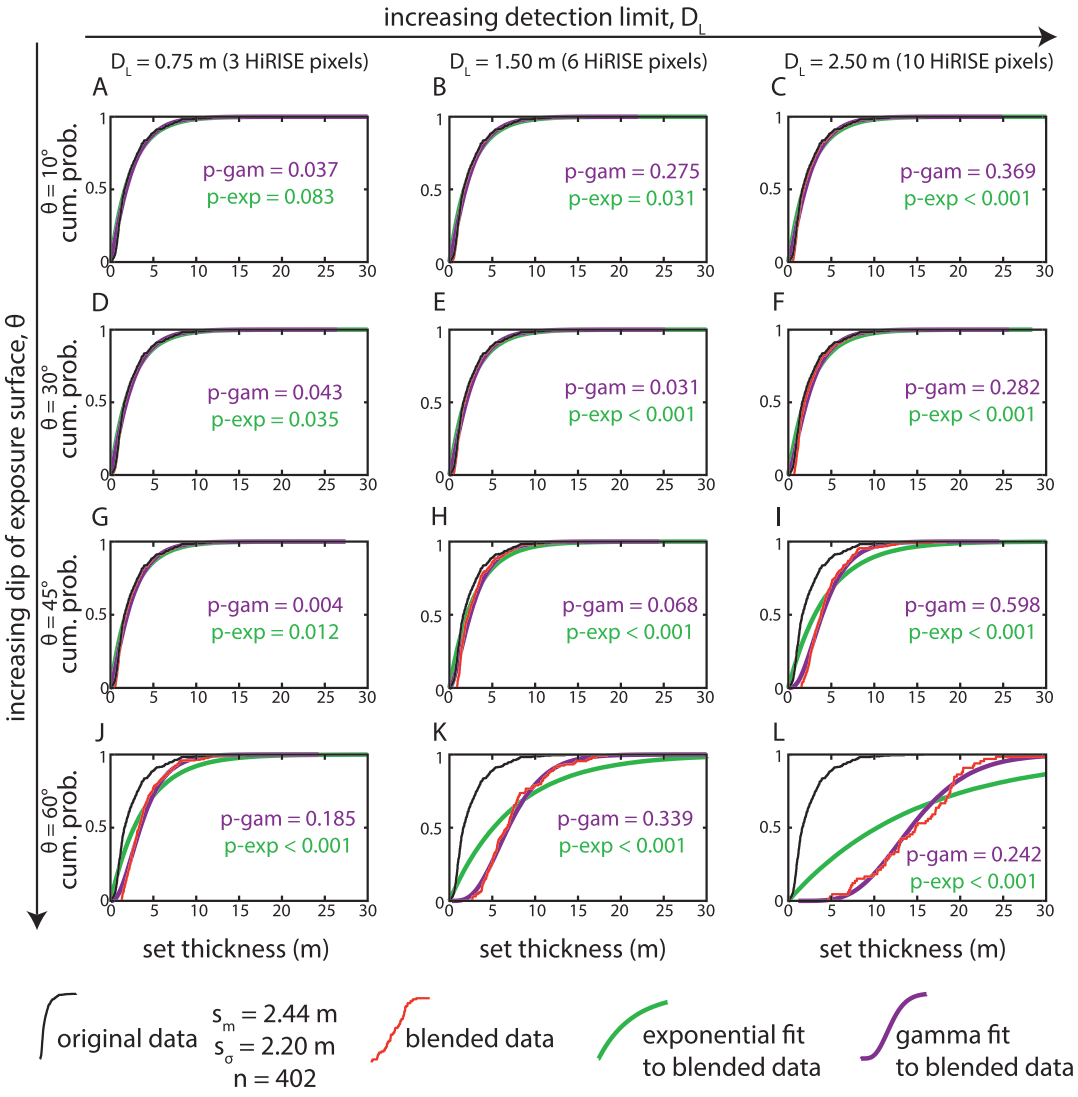

Figure 4. (a–l) Cumulative distribution functions (CDFs) comparing blended data to fitted exponential and gamma curves, as well as the original data set (each panel shows the same data shown in Figure 2). The blending of sets was performed as a function of outcrop dip and assumed detection limits (Figure 1). Shown in these panels are the *p* values from the two-sample Kolmogorov-Smirnov test of similarity between the blended data and the fitted gamma and exponential distributions. The blended data's mean, standard deviation, and *n* values are shown in the associated panels of Figure 2. Columns represent experimental results at detection limits (D_L) = 0.75, 1.50, and 2.50 m (3, 6, and 10 HiRISE pixels). Rows represents results at exposure dips (θ) of 10°, 15°, 30°, and 60°. The progressive blending of sets coincides with the continued departure from the statistical moments of the original data, as well as the change in shape to gamma distributed, which was maintained in all the experiments.

thinner histogram bars in Figure 3, as well as an increase in the mean set thickness. The decrease in *n* eventually leads to a significant reshaping of the distribution, seen clearly in the histograms (Figure 3) and cumulative distribution functions (CDFs, Figure 4) both as outcrop dip and detection limit increase. At any given detection limit, the decrease in *n* and associated distribution reshaping occurs progressively from shallower to steeper surface dips (Figures 3 and 4). In addition to the visual comparison, the similarity of the blended data set to the original is reported with a *p* value produced by a two-sample Kolmogorov-Smirnov test. This is shown across the entire experimental domain in Figure 5, which contours the *p* value results of all experiments at common critical *p* values (0.001, 0.01, and 0.1).

The blended histograms become increasingly gamma shaped with decreasing *n*, driven by the reduction in the thinnest end of the distribution, the increase in the mean and mode, and the thickening tails (Figure 3). The comparison of the blended data sets to the fitted distributions is more clearly made in the CDFs (Figure 4). The progressive blending of sets and decrease in *n* reduces the quality of the exponential fit,

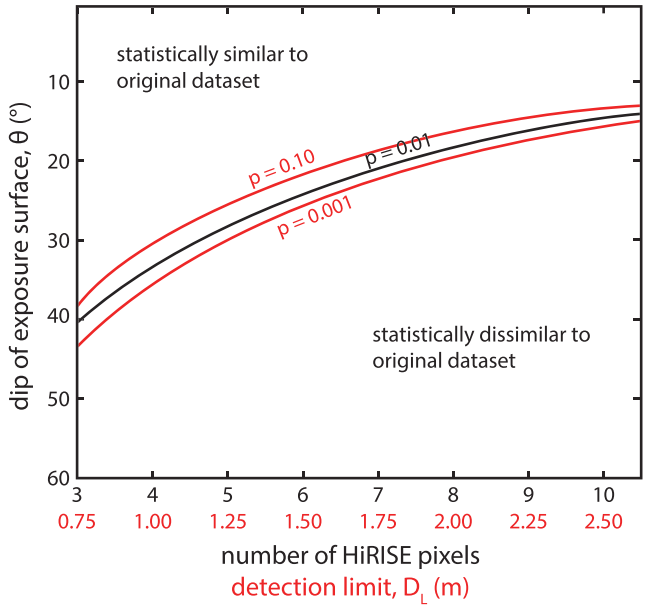

Figure 5. The detection limit (D_L) and the dip of the exposure surface (θ) as controls on the statistical similarity of blended data sets to the original. The red and black lines are contours at p values of 0.10, 0.01, and 0.001 calculated from a two-sample Kolmogorov-Smirnov test. These p values are commonly used as critical p values for rejecting the similarity of two data sets or not.

seen visually and with p values, but maintains and even increases the quality of the gamma fit (Figure 4). The blending also causes s_m to increase by as much as 610% in the most blended data set (Figure 3l), while s_σ only increases by 249% (Figures 3a vs 3l and 6). The difference in sensitivity of these two parameters to the applied blending has significant implications for c_v values (equation 1). The rapid increase in s_m relative to the slow increase in s_σ creates a steady decrease in c_v with decreasing n (Figure 6). Figure 7 shows c_v as a function of the detection limit (D_L) for a number of outcrop dips (θ) ranging from 10° to 60°. These curves are compared to horizontal lines representing the original field measurements from the middle Page (Cardenas et al., 2019) and the Entrada (Crabaugh & Kocurek, 1993; Kocurek & Day, 2018). As D_L and θ increase, steeper outcrop dips deviate from Page values toward Entrada values, while shallow outcrop dips buffer the amount of data loss and change in c_v.

4. Discussion

The results show that there is a significant risk of remote sensing cross-set thickness measurements not representing the actual stratigraphy, and also that there is a clear range of reasonable conditions for measurement of aeolian cross strata from satellite images (Figure 5). Even at 2.50-m (10 HiRISE pixels) detection limits (equation 3), 10° dips (θ) do little to alter the original data set, losing only up to the finest 4% of measurements (Figures 2 and 3a–3c). The preservation of measurements leads to the preservation of reconstructions of dune field kinematics and dune heights, as the c_v of all blended Page data sets at $\theta = 10°$ remains within net-bypass range (Figure 7), consistent with interpretations of the original data set (Cardenas et al., 2019). A 30° dip is able to provide a meaningful

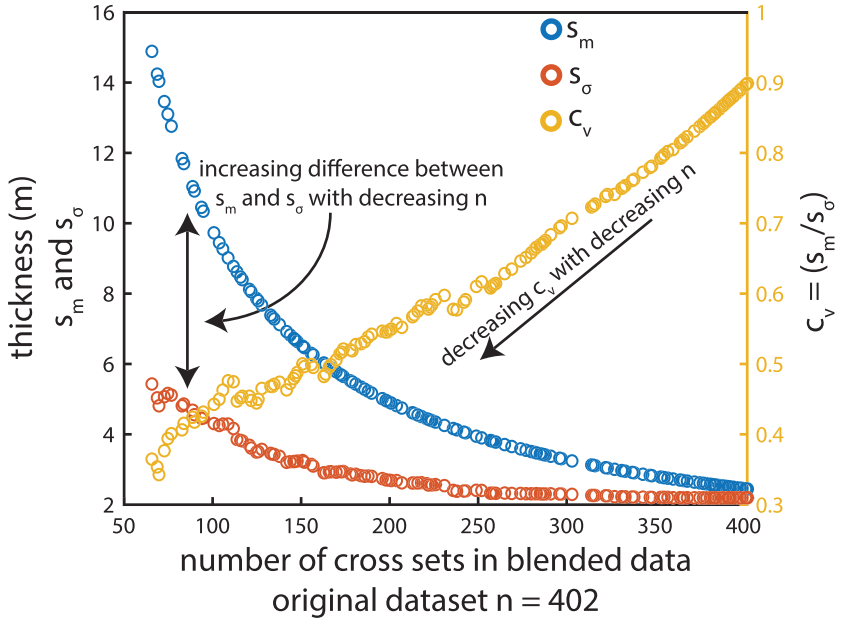

Figure 6. Change in mean set thickness (s_m), standard deviation of set thickness (s_σ), and coefficient of variation of set thickness ($c_v = s_m/s_\sigma$) as a function of the number of detected cross sets (n) in the blended data sets. As n decreases with increased blending, s_m increases more rapidly than s_σ, causing a drop in c_v. The c_v is an important value for reconstructing the history of aeolian dune fields from preserved cross sets, and the change in c_v seen over this plot is significant enough to alter that reconstruction.

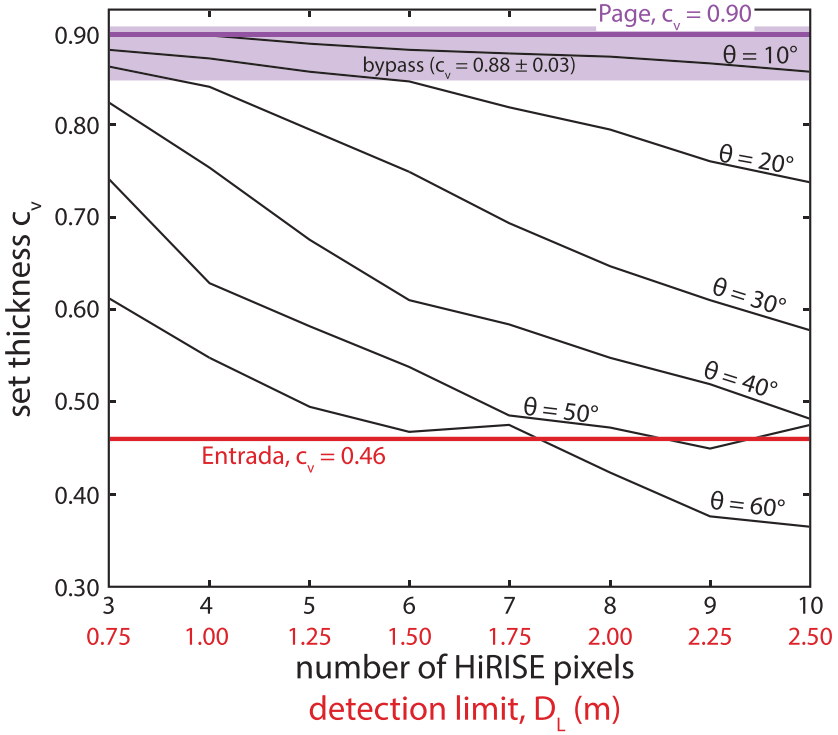

Figure 7. The detection limit, D_L (equation 2), versus the coefficient of variation, c_v (equation 1), of blended and original data sets. The c_v of the unblended Page and Entrada data (Cardenas et al., 2019; Kocurek & Day, 2018) are shown with bold colored lines. A range of c_v values representing net bypass is shown in the purple area (0.88 ± 0.03, Paola & Borgman, 1991; Bridge, 1997). Lower c_v values are increasingly interpreted as aggradational dune fields (Bridge & Best, 1997; Jerolmack & Mohrig, 2005). The Page and Entrada represent opposite types of dune field accumulations (dry and net bypassing vs wet and aggrading). This is represented by their different c_v values. Black lines represent the c_v of the blended Page data sets at different outcrop dips (θ) and D_L values. Increasing detection limits decrease the blended c_v only slightly at $\theta = 10°$ and in fact does not leave the range of net bypass. The effect is more significant at all higher dips. The c_v of $\theta = 20°$ and 30° are within the range of net bypass at $D_L = 0.75$ and 1.25 m but move beyond net-bypass range at higher D_L. At $\theta = 40°$ to 60°, c_v values are lower than net bypass, even at $D_L = 0.75$ m. The c_v of $\theta = 50°$ and 60° is equal to or less than the Entrada c_v at $D_L = 2.00$ and 2.25 m, representing the complete loss of data quality that would lead to the end-member misinterpretation of the Page accumulation history.

measurement at a 0.75 m (three HiRISE pixels) detection limit, with $n = 96\%$ of the original data set (Figures 3 and 7), but not beyond; at $D_L = 1.00$ m (four HiRISE pixels), the 30° dip moves beyond net bypass (Figure 7) and only maintains $n = 82\%$ of the original data. This degree of blending has significantly altered the shape of the fitted distribution, leading to the rejection of an exponential fit (Figures 4g and 4h). In terms of statistical similarity to the original data set, only $\theta \leq 13°$ produced accurate measurements at all D_L (Figure 5). Given the difficulty in truly knowing a detection limit for adjacent aeolian cross sets that may only be subtly visually distinct, focusing on outcrops sloping ≤13°, or at least as shallowly as possible, is likely to result in the data set most accurately representing the actual strata.

Cross-set blending becomes increasingly destructive to Page dune-field reconstructions with decreasing n. Much of this stems from the difference in response to the blending by s_m and s_σ (Figure 6). This indicates that the loss of data alters the shape of the fitted distribution, rather than simply translating it toward thicker measurements (Figures 3 and 4). At worst, the low c_v values and the well-fit gamma curves would lead to the incorrect reconstruction of the middle Page dune fields as highly aggradational (Figure 7), which would in turn lead to discussion regarding the environmental forcings driving aggradation instead of net bypass (e.g., local topography, water table, changing wind regime; Kocurek & Day, 2018; Swanson et al., 2019; Cardenas et al., 2019). In the most blended examples, the 30°, 45°, and 60° exposures have c_v values approaching that of parts of the Entrada Sandstone ($c_v = 0.46$, Figure 7), a wet, aggradational dune field that represents the end-member of aeolian dune field accumulation styles completely opposite to the dry, net bypass of the Page

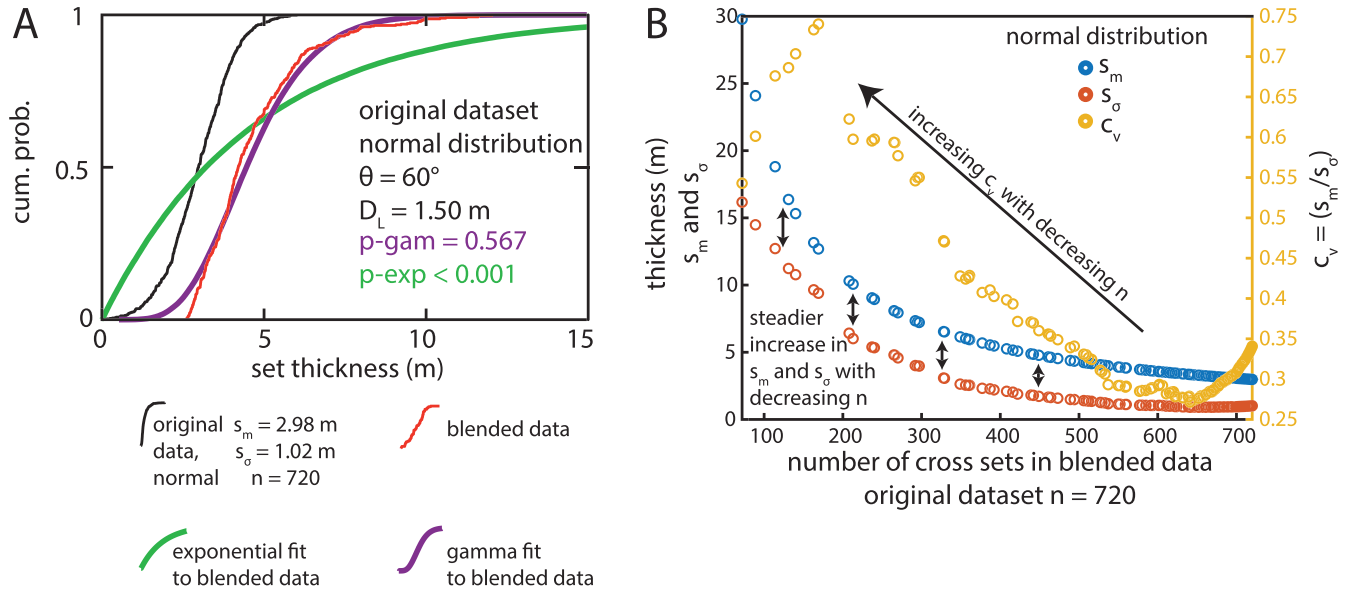

Figure 8. A normal distribution of cross sets run through the same experiments as the Page sets, with the intention of looking for unique responses to the blending process. (a) CDF plot comparing the original normal data set to a blended data set, and the blended data set's fitted exponential and gamma distributions. *P* values are shown for the fits to the blended data. Similar to the Page sets, blending produces a data set that is gamma shaped rather than exponential. (b) Plot comparing the mean set thickness (s_m), standard deviation of set thickness (s_σ), and coefficient of variation of set thickness ($c_v = s_m/s_\sigma$) of the normal distribution in Figure 8a as functions of the number of sets in an experiment, n. Unlike the exponentially distributed Page sets (Figure 6), the normal sets show a steady increase in both s_m and s_σ, which creates a steady increase in c_v.

(Crabaugh & Kocurek, 1993; Havholm et al., 1993; Havholm & Kocurek, 1994). The reconstruction of the Page as an Entrada-type dune field represents a significant departure of the blended data set from the original measurements. Additionally, with a c_v well below 0.88, the ability to reconstruct the distribution of dune heights following the methodology of Cardenas et al. (2019) is lost.

Stack et al. (2013), in their Figure 14, show several examples of bed-thickness distributions from sedimentary outcrop on Mars. These distributions have shapes similar to our high-θ experimental results. Namely, the exponential fits to their measurements underestimate the number of thin beds and overestimate of the number of thick beds (Figures 3i–3l). This is particularly apparent in several of their distributions measured in Holden crater, particularly those labeled H1, H3, H4–H8, and H10 in their Figure 14. Some of the local mean bed thicknesses in Holden crater reported in Stack et al. (2013), and in Henry crater reported in Day and Catling (2019), are within the D_L values tested here. Although these beds have distribution shapes similar to the blended data sets reported here, it is not definitive enough to constrain whether or not the beds in Henry and Holden craters are aeolian cross sets. In Henry crater, recent studies support this hypothesis (Day & Catling, 2019).

The experiments performed here have additional implications for constraining the depositional environment of strata on Mars. Gamma and exponentially distributed cross-set thicknesses, which should represent most aeolian cross sets, have been shown here to increase in mean set thickness (s_m) more rapidly than in standard deviation (s_σ) as blending increases and the number of detected sets, n, decreases. This is not a characteristic shared by all distributions. Figure 8a shows the CDF of a normal distribution, generated randomly with $n = 720$, $s_m = 2.98$ m, and $s_\sigma = 1.02$ m, such that it did not produce negative values and is in range to be modified by the previously used values of θ and D_L. Figure 8a compares this original distribution to the blended distribution at $\theta = 60°$ and $D_L = 1.50$ m. The comparisons are qualitatively similar to the blended Page data sets, and the p values from a two-sample Kolmogorov-Smirnov test would similarly lead to rejection an exponential fit but do not reject a gamma fit (Figure 4). A fit to a normal distribution is rejected as well using the same test ($p < 0.001$). A significant departure of the normal distribution from the Page Sandstone results is that s_m and s_σ increase at a much more similar rate with decreasing n, leading to a c_v that starts low and increases with decreasing n (Figure 8b). By beginning with remote sensing set

thicknesses rather than field measurements, this experiment could presumably be picked up somewhere at a middling n value to test the response of s_m, s_σ, and c_v to decreasing n. An increasing or steady c_v would then be diagnostic of a normal parent distribution, which would likely rule out aeolian origin, although a decreasing c_v pointing toward a parent gamma or exponential distribution would not be unique to aeolian cross sets.

This method and these numerical experiments assume individual cross sets are uniform in thickness at the location of each vertical section. That is, the measured thickness does not change with changing θ. However, during deposition, dune scour depth may vary and thus cause set thickness to vary in a vertical section with changing θ. If such variation in set thickness is present, the possible error associated with the presented workflow is correlated with both the magnitude of set thickness variability and the surface dip used to calculate the excursion distance. Though the potential to alter a single measurement is clear, it is unknown if the statistical moments of the entire population of set-thickness measurements would be altered. Future work is planned to explore the sensitivity of set-thickness measurements to the three dimensionality of dune deposits with variable scour depths using a numerical model (Swanson et al., 2019).

5. Conclusion

As a community, we are in a good technological position to significantly improve our understanding of Mars' aeolian history, as aeolian deposits are far more likely to have bed thicknesses measurable with satellite observations than fluvial or submarine strata. An understanding of the sedimentology down to the scale of individual beds, regardless of depositional setting, is fundamental to paleo-environmental reconstructions. The results of the numerical experiment conducted here are specific to the Page Sandstone but offer a general framework to address problems surrounding the finite size of pixels in remotely collected raster images and irregular outcrop topography when measuring strata thicknesses on Mars. Where possible, measurements should be made from shallow-sloping ($\leq 13°$) outcrops, such that thin sets are fully represented because they are exposed over long distances. The experiments here may also prove useful in reconstructing the original distribution of sets by testing the response of a remotely measured data set to further blending. Finally, with many considering that aeolian strata may compose more of Mars' rock record than previously recognized (e.g., Anderson et al., 2018; Day & Catling, 2019; Grotzinger & Milliken, 2012), this work provides strong quantitative tools with which to interpret these strata and to understand possible sources of error.

Acknowledgments
We would like to thank Editor A. Deanne Rogers and reviewers Kenzie Day and Steve Banham for their constructive comments on this manuscript. An early version of this work benefited from a discussion with Katie Stack Morgan. B. T. C. acknowledges support from the RioMar industry consortium and a University of Texas Graduate School fellowship. Data are available at Caltech's Research Data Repository (https://doi.org/10.22002/d1.1304).

References

Allen, J. R. L. (1973). A classification of climbing-ripple cross-lamination. *Journal of the Geological Society*, *129*(5), 537–541. https://doi.org/10.1144/gsjgs.129.5.0537

Anderson, R. B., Edgar, L. A., Rubin, D. M., Lewis, K. W., & Newman, C. (2018). Complex bedding geometry in the upper portion of Aeolis Mons, Gale Crater, Mars. *Icarus*, *314*, 246–264. https://doi.org/10.1016/j.icarus.2018.06.009

Banham, S. G., Gupta, S., Rubin, D. M., Watkins, J. A., Sumner, D. Y., Edgett, K. S., et al. (2018). Ancient Martian aeolian processes and palaeomorphology reconstructed from the Stimson formation on the lower slope of Aeolis Mons, Gale crater, Mars. *Sedimentology*, *65*(4), 993–1042. https://doi.org/10.1111/sed.12469

Blakey, R. C., Havholm, K. G., & Jones, L. S. (1996). Stratigraphic analysis of eolian interactions with marine and fluvial deposits, Middle Jurassic Page Sandstone and Carmel Formation, Colorado Plateau, USA. *Journal of Sedimentary Research*, *66*, 324–342.

Bridge, J. (1997). Thickness of sets of cross strata and planar strata as a function of formative bed-wave geometry and migration, and aggradation rate. *Geology*, *25*(11), 971–974. https://doi.org/10.1130/0091-7613(1997)025<0971:TOSOCS>2.3.CO;2

Bridge, J., & Best, J. (1997). Preservation of planar laminae due to migration of low-relief bed waves over aggrading upper-stage plane beds: Comparison of experimental data with theory. *Sedimentology*, *44*(2), 253–262. https://doi.org/10.1111/j.1365-3091.1997.tb01523.x

Brothers, S. C., Kocurek, G., Brothers, T. C., & Buynevich, I. V. (2016). Stratigraphic architecture resulting from dune interactions: White Sands Dune Field, New Mexico. *Sedimentology*, *64*, 686–713.

Cardenas, B. T., Kocurek, G., Mohrig, D., Swanson, T., Hughes, C. M., & Brothers, S. C. (2019). Autogenic processes and allogenic forcings preserved in set-scale aeolian stratigraphy II: The scour-and-fill dominated Jurassic Page Sandstone, Arizona, USA. *Journal of Sedimentary Research*, *89*(8), 741–760. https://doi.org/10.2110/jsr.2019.41

Chojnacki, M., Banks, M. E., Fenton, L. K., & Urso, A. C. (2019). Boundary condition controls on the high-sand-flux regions of Mars. *Geology*, *47*(5), 427–430. https://doi.org/10.1130/G45793.1

Chojnacki, M., Johnson, J. R., Moersch, J. E., Fenton, L. K., Michaels, T. I., & Bell, J. F. III (2015). Persistent aeolian activity at Endeavour crater, Meridiani Planum, Mars: new observations from orbit and the surface. *Icarus*, *251*, 275–290. https://doi.org/10.1016/j.icarus.2014.04.044

Cornwall, C., Bourke, M. C., Jackson, D. W. T., & Cooper, J. A. G. (2018). Aeolian slipface dynamics and grainflow morphologies on Earth and Mars. *Icarus*, *314*, 311–326. https://doi.org/10.1016/j.icarus.2018.05.033

Cornwall, C., Jackson, D. W. T., Bourke, M. C., & Cooper, J. A. G. (2018). Morphometric analysis of slipface processes of an aeolian dune: Implications for grain-flow dynamics. *Sedimentology*, *65*(6), 2034–2054. https://doi.org/10.1111/sed.12456

Crabaugh, M., & Kocurek, G. (1993). Entrada Sandstone: an example of a wet aeolian system. *Geological Society, London, Special Publications*, *72*(1), 103–126. https://doi.org/10.1144/gsl.sp.1993.072.01.11

Day, M. D., & Catling, D. C. (2018). Dune casts preserved by partial burial: The first identification of ghost dune pits on Mars. *Journal of Geophysical Research: Planets*, *123*(6), 1431–1448. https://doi.org/10.1029/2018je005613

Day, M. D., & Catling, D. C. (2019). Potential aeolian deposition of intra-crater layering: A case study of Henry crater, Mars. *Geological Society of America Bulletin*. https://doi.org/10.1130/B35230.1

Day, M. D., & Kocurek, G. (2016). Observations of an aeolian landscape: From surface to orbit in Gale crater. *Icarus*, *280*, 37–71. https://doi.org/10.1016/j.icarus.2015.09.042

Day, M. D., & Kocurek, G. (2017). Aeolian dune interactions preserved in the ancient rock record. *Sedimentary Geology*, *358*, 187–196. https://doi.org/10.1016/j.sedgeo.2017.07.009

Day, M. D., & Kocurek, G. (2018). Pattern similarity across planetary dune fields. *Geology*, *46*(11), 999–1002. https://doi.org/10.1130/G45547.1

Ewing, R. C., & Kocurek, G. (2010a). Aeolian dune-field pattern boundary conditions. *Geomorphology*, *114*(3), 175–187. https://doi.org/10.1016/j.geomorph.2009.06.015

Ewing, R. C., & Kocurek, G. (2010b). Aeolian dune interactions and dune-field pattern formation: White Sands Dune Field, New Mexico. *Sedimentology*, *57*, 1199–1219.

Ewing, R. C., McDonald, G. D., & Hayes, A. G. (2015). Multi-spatial analysis of aeolian dune-field patterns. *Geomorphology*, *240*, 44–53. https://doi.org/10.1016/j.geomorph.2014.11.023

Ewing, R. C., Peyret, A.-P. B., Kocurek, G., & Bourke, M. (2010). Dune field pattern formation and recent transporting winds in the Olympia Undae dune field, north polar region of Mars. *Journal of Geophysical Research - Planets*, *115*, E08005. https://doi.org/10.1029/2009JE003526

Fenton, L. K., & Hayward, R. K. (2010). Southern high latitude dune fields on Mars: Morphology, aeolian inactivity, and climate change. *Geomorphology*, *121*(1-2), 98–121. https://doi.org/10.1016/j.geomorph.2009.11.006

Ganti, V., Paola, C., & Foufoula-Georgiou, E. (2013). Kinematic controls on the geometry of the preserved cross sets. *Journal of Geophysical Research: Earth Surface*, *118*, 1296–1307. https://doi.org/10.1002/jgrf.20094

Goudge, T. A., Milliken, R. E., Head, J. W., Mustard, J. F., & Fassett, C. I. (2017). Sedimentological evidence for a deltaic origin of the western fan deposit in Jezero craters, Mars and implications for future exploration. *Earth and Planetary Science Letters*, *458*, 357–365. https://doi.org/10.1016/j.epsl.2016.10.056

Grotzinger, J. P., Arvidson, R. E., Bell, J. F. III, Calvin, W., Clark, B. C., Fike, D. A., et al. (2005). Stratigraphy and sedimentology of a dry to wet eolian depositional system, Burns formation, Meridiani Planum, Mars. *Earth and Planetary Science Letters*, *240*(1), 11–72. https://doi.org/10.1016/j.epsl.2005.09.039

Grotzinger, J. P., & Milliken, R. E. (2012). The sedimentary rock record of Mars: Distribution, origins, and global stratigraphy. In J. P. Grotzinger, & R. E. Milliken (Eds.), *Sedimentary Geology of Mars, SEPM Special Publication* (Vol. 102, pp. 1–48). Tulsa, Oklahoma: SEPM.

Havholm, K. G., Blakey, R. C., Capps, M., Jones, L. S., King, D. D., & Kocurek, G. (1993). Aeolian genetic stratigraphy: An example from the Middle Jurassic Page sandstone, Colorado Plateau. In K. Pye, & N. Lancaster (Eds.), *Aeolian Sediments: Ancient and Modern International Association of Sedimentologists Special Publication*, (Vol. 16, pp. 87–107). Oxford: Blackwell Scientific Publications. https://doi.org/10.1002/9781444303971.ch7

Havholm, K. G., & Kocurek, G. (1994). Factors controlling aeolian sequence stratigraphy: Clues from super bounding surface features in the Middle Jurassic Page Sandstone. *Sedimentology*, *41*(5), 913–934. https://doi.org/10.1111/j.1365-3091.1994.tb01432.x

Hughes, C. M., Cardenas, B. T., Goudge, T. A., & Mohrig, D. (2019). Deltaic deposits indicative of a paleo-coastline at Aeolis Dorsa, Mars. *Icarus*, *317*, 442–453. https://doi.org/10.1016/j.icarus.2018.08.009

Jerolmack, D. J., & Mohrig, D. (2005). Frozen dynamics of migrating bedforms. *Geology*, *33*(1), 57–60. https://doi.org/10.1130/G20897.1

Kirk, R. L., Howington-Kraus, E., Rosiek, M. R., Anderson, J. A., Archinal, B. A., Becker, K. J., et al. (2008). Ultrahigh resolution topographic mapping of Mars with MRO HiRISE stereo images: Meter-scale slopes of candidate Phoenix landing sites. *Journal of Geophysical Research - Planets*, *113*, E00A24. https://doi.org/10.1029/2007JE003000

Kite, E. S., Lewis, K. W., Lamb, M. P., Newman, C. E., & Richardson, M. I. (2013). Growth and form of the mound in Gale crater, Mars: Slope wind enhanced erosion and transport. *Geology*, *41*(5), 543–546. https://doi.org/10.1130/G33909.1

Kite, E. S., Sneed, J., Mayer, D. P., Lewis, K. W., Michaels, T. I., Hore, A., & Rafkin, S. C. R. (2016). Evolution of major sedimentary mounds on Mars: Buildup via anticompensational stacking modulated by climate change. *Journal of Geophysical Research: Planets*, *121*, 2282–2324. https://doi.org/10.1002/2016JE005135

Kocurek, G., & Day, M. D. (2018). What is preserved in the aeolian rock record? A Jurassic Entrada sandstone case study at the Utah–Arizona border. *Sedimentology*, *65*(4), 1301–1321. https://doi.org/10.1111/sed.12422

Kocurek, G., Ewing, R. C., & Mohrig, D. (2010). How do bedform patterns arise? New views on the role of bedform interactions within a set of boundary conditions. *Earth Surface Processes and Landforms*, *35*(1), 51–63. https://doi.org/10.1002/esp.1913

Lapotre, M. G. A., Ewing, R. C., Lamb, M. P., Fischer, W. W., Grotzinger, J. P., Rubin, D. M., et al. (2016). Large wind ripples on Mars: A record of atmospheric evolution. *Science*, *353*(6294), 55–58. https://doi.org/10.1126/science.aaf3206

Leclair, S. F., Bridge, J. S., & Wang, F. (1997). Preservation of cross-strata due to migration of subaqueous dunes over aggrading and non-aggrading beds: comparison of experimental data with theory. *Geoscience Canada*, *24*, 55–66.

Lewis, K. W., Aharonson, O., Grotzinger, J. P., Kirk, R. L., McEwen, A. S., & Suer, T.-A. (2008). Quasi-periodic bedding in the sedimentary rock record of Mars. *Science*, *322*(5907), 1532–1535. https://doi.org/10.1126/science.1161870

Lewis, K. W., Aharonson, O., Grotzinger, J. P., Squyres, S. W., Bell, J. F. III, Crumpler, L. S., & Schmidt, M. E. (2008). Structure and stratigraphy of Home Plate from the Spirit Mars Exploration Rover. *Journal of Geophysical Research*, *113*(E12), E12S36. https://doi.org/10.1029/2007JE003025

Loope, D. B. (2006). Dry-season tracks in dinosaur-triggered grianflows. *Palaios*, *21*(2), 132–142. https://doi.org/10.2110/palo.2005.p05-55

McEwen, A. S., Eliason, E. M., Bergstrom, J. W., Bridges, N. T., Hansen, C. J., Delamere, W. A., et al. (2007). Mars Reconnaissance Orbiter's High Resolution Imaging Science Experiment (HiRISE). *Journal of Geophysical Research - Planets*, *112*, E05S02. https://doi.org/10.1029/2005JE002605

Milliken, R. E., Ewing, R. C., Fischer, W. W., & Hurowitz, J. (2014). Wind-blown sandstones cemented by sulfate and clay minerals in Gale crater, Mars. *Geophysical Research Letters*, *41*, 1149–1154. https://doi.org/10.1002/2013GL059097

Paola, C., & Borgman, L. (1991). Reconstructing random topography from preserved stratification. *Sedimentology*, *38*(4), 553–565. https://doi.org/10.1111/j.1365-3091.1991.tb01008.x

Rodríguez-López, J. P., Clemmensen, L. B., Lancaster, N., Mountney, N. P., & Veiga, G. D. (2014). Archean to Recent aeolian sand systems and their sedimentary record: Current understanding and future prospects. *Sedimentology*, *61*(6), 1487–1534. https://doi.org/10.1111/sed.12123

Rubin, D. M., & Hunter, R. E. (1982). Bedform climbing in theory and nature. *Sedimentology*, *29*(1), 121–138. https://doi.org/10.1111/j.1365-3091.1982.tb01714.x

Rubin, D. M., & Hunter, R. E. (1983). Reconstructing bedform assemblages from compound crossbedding. In M. E. Brookfield, & T. S. Ahlbrandt (Eds.), *Eolian Sediments and Processes Developments in Sedimentology*, (Vol. 38, pp. 407–427). Amsterdam - Oxford - New York - Tokyo: Elsevier. https://doi.org/10.1016/S0070-4571(08)70807-0

Silvestro, S., Vaz, D. A., Ewing, R. C., Rossi, A. P., Fenton, L. K., Michaels, T. I., et al. (2013). Pervasive aeolian activity along rover Curiosity's traverse in Gale Crater, Mars. *Geology*, *41*(4), 483–486. https://doi.org/10.1130/G34162.1

Silvestro, S., Vaz, D. A., Fenton, L. K., & Geissler, P. E. (2011). Active aeolian processes on Mars: A regional study in Arabia and Meridiani Terrae. *Geophysical Research Letters*, *38*, L20201. https://doi.org/10.1029/2011GL048955

Stack, K. M., Grotzinger, J. P., & Milliken, R. E. (2013). Bed thickness distributions on Mars: An orbital perspective. *Journal of Geophysical Research: Planets*, *118*, 1323–1349. https://doi.org/10.1002/jgre.20092

Swanson, T., Mohrig, D., & Kocurek, G. (2016). Aeolian dune sediment flux variability over an annual cycle of wind. *Sedimentology*, *63*(6), 1753–1764. https://doi.org/10.1111/sed.12287

Swanson, T., Mohrig, D., Kocurek, G., Cardenas, B. T., & Wolinsky, M. A. (2019). Autogenic processes and allogenic forcings preserved in set-scale aeolian stratigraphy I: Numerical experiments. *Journal of Sedimentary Research*, *89*(8), 728–740. https://doi.org/10.2110/jsr.2019.42

van der Mark, C. F., Blom, A., & Hulscher, S. J. M. H. (2008). Quantification of variability in bedform geometry. *Journal of Geophysical Research*, *113*(F3), F03020. https://doi.org/10.1029/2007JF000940